International Journal of Heat and Mass Transfer 240 (2025) 126639

Contents lists available at ScienceDirect

International Journal of Heat and Mass Transfer

journal homepage: www.elsevier.com/locate/ijhmt

Environmental-structural-structural heat transfer characteristics analysis of an assembled power turbine rotor system

Yazheng Zhao, Jin Zhou *, Mingjie Guo, Yuanping Xu

College of Mechanical and Electrical Engineering, Nanjing University of Aeronautics and Astronautics, Nanjing, 210016, China

A R T I C L E I N F O

Keywords:
Power turbine rotor
Assembly system
Heat transfer
Environmental-structural-structural

A B S T R A C T

Currently, research on the heat transfer characteristics of high-speed assembled power turbine rotor system primarily focuses on the convective heat transfer between environment and rotor structure, and often ignores the heat conduction between the structure and structure. However, the operating parameters related to the working conditions and the interface parameters between structures actually have a synergistic effect on the temperature, and neglecting structural-structural heat conduction may result in localized overheating. In addition, parameter thresholds have not been fully discussed. Herein, this study innovatively integrates the coupling effects of operating and assembly interface parameters on environmental-structural-structural heat transfer characteristics in power turbine rotors, and identifies thresholds of parameters influencing thermal performance and their relationships with temperature. First, an environmental-structural-structural heat transfer model is constructed based on fractal theory and finite element method. This model takes into account the effects of operating parameters related to the working conditions, as well as interface parameters related to the assembly state. Then, the influences of key factors including rotational speed, rotational Reynolds number, tightening torque, interface contact area, number of bolts, and surface topography on the environmental-structural-structural heat transfer characteristics are elaborated. It is found that the operating parameters have an exponential relationship with temperature, and their threshold are determined by fluid characteristics, boundary layer thickness and centrifugal force. The tightening torque influences heat transfer characteristics by altering the contact thermal conductance, with a noticeable threshold below which heat transfer performance decreases. This work provides valuable insights into heat transfer dynamics of assembled power turbine rotor systems, contributing to more accurate thermal management strategies in high-speed turbine applications.

1. Introduction

Aero-engine power turbine rotors, characterized by bolted drum structures, generally operate in complex, high-temperature environments for extended periods [1–5]. The temperature distribution within rotors significantly affects thermal stress, which in turn influences the thermoelastic coupling and vibration characteristics, ultimately impacting the reliability of rotor [6–8]. Therefore, a thorough understanding of the heat transfer characteristics of aero-engine turbine rotors is essential for effective thermal management and optimization of design parameters.

Substantial attempts have been made to explore the heat transfer characteristics of aero-engine rotor. For instance, Zou et al. [9] analyzed how geometric configurations and operational parameters affect the heat transfer of the turbine rotor. Qian et al. [10] conducted a comparative study on heat transfer performance under static and rotating conditions. The work by Hu et al. [11] highlighted the impact of geometric factors, such as curvature and surface area on cooling efficiency. Owen et al. [12] provided foundational knowledge on the convective heat transfer characteristics of free disks through extensive experimental investigations. Lin et al. [13] performed a comprehensive evaluation of heat transfer performance in a high-speed rotating free disk system. Ghasemian et al. [14] conducted an investigation on the influence of flow characteristics on heat transfer characteristics. Owen et al. [15] reviewed buoyancy-induced flows in closed rotating cavities and open cavities with air inflow, providing insights into how buoyancy affects heat transfer rates. Lin et al. [16] explored the effects of various factors, including rotational Reynolds and Mach numbers, on the heat transfer performance of disk cavities within rotor-stator systems. Liao et al. [17] discussed how different gap ratios influence system

* Corresponding author.
E-mail address: zhj@nuaa.edu.cn (J. Zhou).

https://doi.org/10.1016/j.ijheatmasstransfer.2024.126639
Received 18 August 2024; Received in revised form 15 December 2024; Accepted 24 December 2024
Available online 30 December 2024
0017-9310/© 2024 Elsevier Ltd. All rights reserved, including those for text and data mining, AI training, and similar technologies.

temperature and heat transfer coefficients. Recent studies [18–23] employing both experimental and numerical methodologies have examined how inlet fluid properties and Reynolds number affect thermal performance. Hu et al. [24] demonstrated that the flow pattern significantly influences heat transfer characteristics. The literatures [25,26] also extensively discussed the relationship between rotational speed and heat transfer coefficients. Creci et al. [27] conducted an environmental-structural heat transfer analysis of a single-shaft gas turbine, which highlighted the importance of considering both thermal and structural integrity in turbine design. Furthermore, the research indicates that turbines with multiple co-rotating or counter-rotating rotors can enhance heat transfer rates due to the formation of an interface layer between the rotating disk [28]. Li et al. [29] introduced a heat soakage model for evaluating heat transfer performance in aero-engines, which is particularly useful for predicting thermal behavior during transient operations.

Overall, significant progress has been made in understanding the heat transfer characteristics of aero-engine turbines. Particularly, attention is predominantly focused on the environmental-structural convective heat transfer, providing valuable insights into how geometric and operational parameters affect thermal performance. However, it should be signified that apart from the environmental-structural convective heat transfer, the structural-structural heat conduction cannot be overlooked [31–36], particularly in the assembly power turbine rotors. This aspect is especially significant in scenarios where high thermal gradients exist within the turbine components, such as in the transition regions between hot and cold sections or in areas with complex geometries that hinder effective heat dissipation. Ignoring structural-structural heat conduction will lead to localized overheating, potentially resulting in thermal fatigue or failure of the components. Furthermore, the interface factors primarily influencing structural-structural heat conduction and the operating factors mainly governing environment-structure convective heat transfer are synergistically affecting the temperature. Given that this mechanism has been rarely investigated, further attempts are still required to explore the environmental-structural-structural heat transfer characteristics in assembled turbine rotors influenced by interface contact parameters. On the other hand, the thresholds of operating and the interface parameters are not sufficiently explored. Identifying these thresholds is essential for precisely evaluating the thermal characteristics of the turbine rotor and remains an ongoing task. Meantime, the quantitative relationship between these key parameters and temperature is not clear.

Therefore, this study conducts an integrated analysis of the coupling effects of operating and assembly interface parameters on environmental-structural-structural heat transfer characteristics in assembled power turbine rotors, uncovering thresholds of critical parameters and relationships with temperature. This is the innovation and main contribution of this work. Specifically, an environmental-structural-structural heat transfer model is firstly developed using fractal theory and the finite element method (FEM). Integrating fractal theory with the finite element method to capture the complex interactions at the interface. This model integrates the complex geometries and varying surface boundary conditions in turbine rotor systems. Making use of this model, the impacts of critical factors including rotational speed, rotational Reynolds number, tightening torque, interface contact area, bolt count and surface topography on environmental-structural-structural heat transfer characteristics are thoroughly analyzed. Based on the analysis, the critical thresholds of operating parameters related to working conditions, including rotational speed and rotational Reynolds number, and their quantitative relationships with temperature are discussed. Furthermore, the main determinants of thermal contact conductivity (TCC), as well as critical thresholds for assembly parameters, are elaborated.

2. The temperature field model of the assembled rotor

The temperature field model of axisymmetric rotor element considering the convective heat transfer between the axisymmetric rotor element and the environment is developed in this section. Subsequently, the thermal resistance model of the bolt interface is derived based on the fractal theory and bolt contact characteristics. The temperature field model of the substructure is assembled through the thermal resistance model to form an environmental-structural-structural temperature model, which is used for subsequent analysis of heat transfer characteristics.

2.1. The temperature field of the axisymmetric rotor element

Given the axisymmetric properties of the turbine rotor in an aero-engine, the circumferential temperature difference is negligible during normal operation. Therefore, as depicted in Fig. 1, the spatial temperature field is simplified into a two-dimensional model that captures the non-uniform temperature distribution in both the axial and radial directions. Consequently, the transient heat transfer partial differential equation of the axisymmetric structure is expressed as follows:

$$\frac{\partial T}{\partial t} = \frac{k}{c_p \rho}\left(\frac{\partial^2 T}{\partial r^2} + \frac{1}{r}\frac{\partial T}{\partial r} + \frac{\partial^2 T}{\partial z^2} + \frac{q_v}{k}\right) \tag{1}$$

where T represents the temperature field, t denotes time, z and r are the axial and radial coordinates of the axisymmetric structure respectively, q_v represents the internal heat source, k denotes the thermal conductivity, c_p represents the constant pressure specific heat, and ρ is the density. The residual function expression is derived as follows:

$$D[T(r,z,t)] = k\left(r\frac{\partial^2 T}{\partial r^2} + \frac{\partial T}{\partial r} + r\frac{\partial^2 T}{\partial z^2}\right) + rq_v - r\rho c_p \frac{\partial T}{\partial t} \tag{2}$$

Furthermore, the following weighted residual formula is obtained based on the Galerkin method.

$$\iint_{DE} W_l\left[k\left(r\frac{\partial^2 T}{\partial r^2} + \frac{\partial T}{\partial r} + r\frac{\partial^2 T}{\partial z^2}\right) + rq_v - r\rho c_p \frac{\partial T}{\partial t}\right] dzdr = 0, (l = 1, 2, \ldots, n) \tag{3}$$

where DE represents the domain of the temperature field, l denotes the node number, and W_l is the weighting function defined as $W_l = \partial T / \partial T_l$. Using the step-by-step integration method and Green's formula, Eq. (3) is formulated as the variational equation for the axisymmetric temperature field.

$$\iint_{D}\left[kr\left(\frac{\partial W_l}{\partial r}\frac{\partial T}{\partial r} + \frac{\partial W_l}{\partial z}\frac{\partial T}{\partial z}\right) - W_l r q_v + W_l r\rho c_p \frac{\partial T}{\partial t}\right] dzdr - \oint_{\Gamma} W_l r k \frac{\partial T}{\partial n} ds = 0, (l = 1, 2, \ldots, n) \tag{4}$$

where Γ is the boundary curve. Triangular elements are utilized to model the temperature field. As shown in Fig. 2, each element E comprises three nodes, represented as $l = (i,j,m)$. The first type of boundaries comprises adiabatic boundaries, internal heat conduction boundaries,

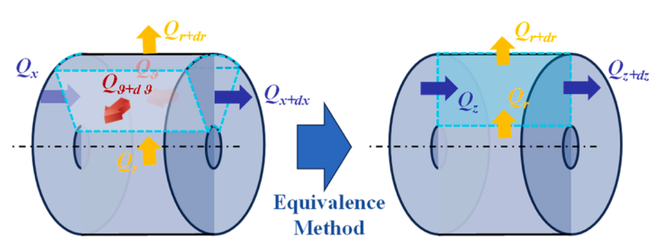

Fig. 1. The simplified method of temperature field.

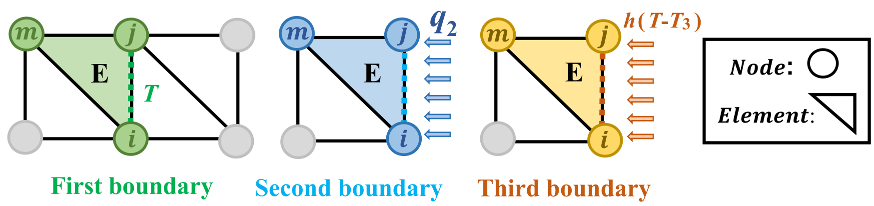

Fig. 2. Three types of boundaries.

and boundaries with temperature T. If the boundary condition for the boundary ij is specified as either heat flux density q_2 or convective heat transfer (the convective heat transfer coefficient h and the temperature T_3), then boundary ij is defined as the second or third type of boundary, respectively.

The variation equations for the axisymmetric temperature field with three boundary conditions are derived from the Eq. (4) and boundary conditions as follows:

$$\begin{cases} \dfrac{\partial J^E}{\partial T_l} = \displaystyle\int\int_E \left[kr\left(\frac{\partial W_l}{\partial r}\frac{\partial T}{\partial r} + \frac{\partial W_l}{\partial z}\frac{\partial T}{\partial z}\right) - W_l r q_v + W_l r \rho c_p \frac{\partial T}{\partial t}\right] dz dr \\ \dfrac{\partial J^E}{\partial T_l} = \displaystyle\int\int_E \left[kr\left(\frac{\partial W_l}{\partial r}\frac{\partial T}{\partial r} + \frac{\partial W_l}{\partial z}\frac{\partial T}{\partial z}\right) - W_l r q_v + W_l r \rho c_p \frac{\partial T}{\partial t}\right] dz dr - \int_{ij} W_l r q_2 ds \\ \dfrac{\partial J^E}{\partial T_l} = \displaystyle\int\int_E \left[kr\left(\frac{\partial W_l}{\partial r}\frac{\partial T}{\partial r} + \frac{\partial W_l}{\partial z}\frac{\partial T}{\partial z}\right) - W_l r q_v + W_l r \rho c_p \frac{\partial T}{\partial t}\right] dz dr \end{cases} \tag{5}$$

It is assumed that the temperature $T(i,j,m)$ at any location within the element is represented by three nodes.

$$T(i,j,m) = [N]^e \left[T_i,\ T_j,\ T_m\right]^{\mathrm{T}} \tag{6}$$

where the shape function is denoted by $[N]^e = [N_i,\ N_j,\ N_m]$, with its specific expression provided in Appendix A. Consequently, the weight function of node l is defined as $W_l = N_l$. By substituting the weight function and the element temperature into Eq. (5), the finite element equation for the temperature field of the axisymmetric rotor element can be derived as follows:

$$[KT]^E\{T\}^E + [NT]^E\left\{\frac{\partial T}{\partial t}\right\}^E = \{PT\}^E \tag{7}$$

Among them, $\{T\}^E$,$\{\partial T/\partial t\}^E$ represent the temperature vector and first-order derivative vector of temperature of an element, respectively. $[KT]^E$, $[NT]^E$, and $\{PT\}^E$ denote the thermal conductivity matrix, heat capacity matrix, and temperature load vector, respectively. The specific expressions can be found in Appendix A.

The backward difference method is employed to solve the temperature field equation. The calculation equation is provided below:

$$\left([KT] + \frac{[NT]}{\Delta t}\right)\{T\}_t = \{PT\}_t + \frac{[NT]}{\Delta t}\{T\}_{t-\Delta t} \tag{8}$$

2.2. Contact heat transfer model for bolted connections

The thermal resistance at the rotor interface encompasses the thermal resistance of all bolted interfaces. Fig. 3 illustrates the thermal resistance equivalent method of contact surface connected by bolts. All thermal resistances are evenly distributed over the nominal contact surface to form an equivalent thermal resistance $\widetilde{R}$ based on the parallel connection property of thermal resistances. This method ensures that the temperature at positions a and b remains consistent before and after equivalence, accurately capturing the temperature gradient caused by the rough bolt contact interface. The TCC model takes into account the interface pressure characteristics of bolted connections.

The equivalent TCC equation between interfaces connected by multiple bolts is given by [30]:

$$\widetilde{h} = \frac{1}{\widetilde{R}A_{face}} = \frac{1}{A_{face}}\sum_{i=1}^{N_{bolt}}\frac{1}{R_{bolti}} \tag{9}$$

where $\widetilde{R}$ represents the equivalent contact thermal resistance, A_{face} denotes the nominal contact area of the entire interface, and N_{bolt} is the number of bolts. R_{bolti} denotes the contact thermal resistance of a single bolt connection interface, with its specific expression provided in [30]:

$$\begin{aligned} R_{bolti} = & \int_{a_s}^{a_{tc}} \frac{\left(\begin{array}{c}\sqrt{\pi a_t A_a}(k_a+k_b)\left(1-\sqrt{\dfrac{A_r}{A_a}}\right)^{1.5} + \\ (k_a+k_b)\sqrt{2A_r}\sigma\left[erfc^{-1}(2P_s) + erfc^{-1}\left(\dfrac{2A_t}{A_a}\right)\right]\end{array}\right)}{2k_a k_b\sqrt{A_a}\ a_t n(a_t)} da_t \\ & + \int_{a_{tc}}^{a_{tmax}} \frac{\left(\begin{array}{c}\sqrt{2\pi A_a a_t}(k_a+k_b)\left(1-\sqrt{\dfrac{A_r}{A_a}}\right)^{1.5} + \\ \sqrt{8A_r}(k_a+k_b)\sigma\left[erfc^{-1}(2P_s) + erfc^{-1}\left(\dfrac{2A_t}{A_a}\right)\right]\end{array}\right)}{2k_a k_b\sqrt{A_a}\ a_t n(a_t)} da_t \end{aligned} \tag{10}$$

where k_a and k_b are the thermal conductivity coefficients of the structures on both sides of the interface respectively. a_t, a_{tmax}, a_{tc}, and a_s denote the truncated area, maximum truncated area, critical truncated

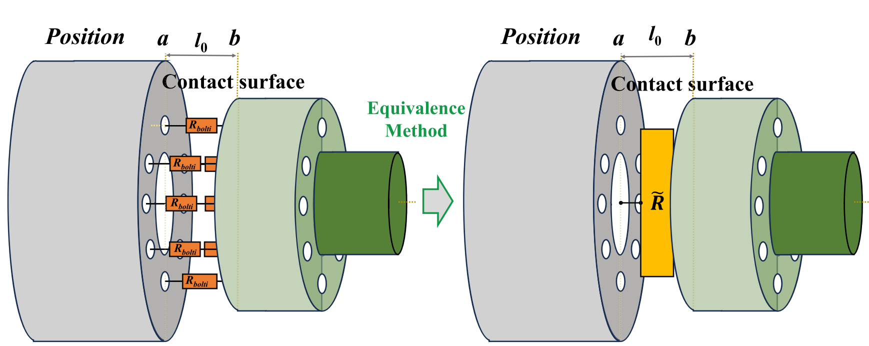

Fig. 3. The thermal resistance equivalent method.

area, and minimum truncated area of the asperity, respectively, with their specific expressions given in Eq. (11). $erfc^{-1}$ represents the inverse function of the complementary error function, σ is the root mean square (RMS) height, P_s is the small probability value, and $n(a_t)$ is the asperity distribution density function, shown in Eq. (12). A_a, A_r, and A_t respectively represent the nominal contact area, the total actual contact area, and the total truncated contact area of a single bolt, as detailed in Eq. (13).

$$\begin{cases} a_{tmax} = A_t D_f^{-1}(2 - D_f)\varphi^{\frac{D_f - 2}{2}} \\ a_{tc} = 2G_f^2 \left(\frac{\widetilde{H}}{2\widetilde{E}}\right)^{\frac{2}{1-D_f}} \\ a_s = 10^{-18} \end{cases} \tag{11}$$

where D_f and G_f denote the fractal dimension and fractal roughness, respectively. $\widetilde{H}$ and $\widetilde{E}$ represent the equivalent hardness and elastic modulus of the contact surface. φ is the domain expansion factor, satisfying the equation $\varphi^{(2-D_f)/2} - \left(1 + \varphi^{-1/2D_f}\right)^{1-2/D_f} - 2/D_f + 1 = 0$, $D_f \in (1, 2)$.

$$n(a_t) = \frac{1}{2} D_f \varphi^{\frac{2-D_f}{2}} a_{tmax}^{\frac{D_f}{2}} a_t^{-\frac{D_f+2}{2}}, a_t \in [0, a_{tmax}] \tag{12}$$

$$\begin{cases} A_a = \pi r_m^2 - \pi\left(\frac{\alpha d}{2}\right)^2 \\ A_r = \frac{1}{2}\int_0^{a_{tmax}} a_t n(a_t) da_t \\ A_t = \int_0^{a_{tmax}} a_t n(a_t) da_t \end{cases} \tag{13}$$

where α denotes the diameter coefficient of the bolt hole, d represents the nominal diameter of the bolt, and r_m is the distance from the center of the bolt hole to the stress field boundary.

As shown in Fig. 4, there is tiny gap between substructures. The heat transfer models of the substructures are assembled through the thermal resistance models to form an environmental-structural-structural temperature model. By this method, operating parameters related to the working condition and interface contact parameters associated with assembly are incorporated into the model.

3. Boundary conditions of T700 power turbine rotor

Boundary conditions are crucial for calculating the environmental-structural-structural heat transfer characteristics of the aero-engine power turbine rotor. Convection is the primary heat transfer method between the environment and the structure, necessitating a detailed analysis of the power turbine rotor cavity characteristics. Heat transfer between structures occurs predominantly through thermal conduction, underscoring the necessity for a detailed analysis of interface characteristics.

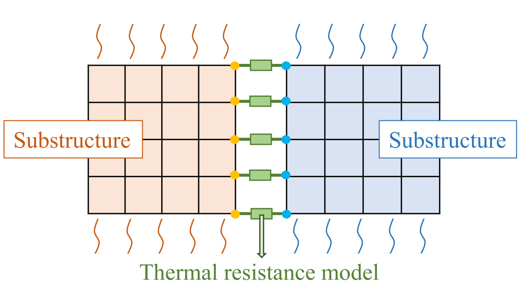

Fig. 4. The assembly method of temperature field.

This section first introduces the equivalent heat transfer rotor. It then analyzes the heat transfer boundary conditions of the hot and cooling surfaces in the convection heat transfer mode. Finally, it presents the interface parameters of the assembled power turbine rotor in the structural-structural heat transfer mode.

3.1. Equivalent heat transfer rotor

Fig. 5 shows the power turbine rotor of the T700 turboshaft engine. The high-temperature gas generated in the combustion chamber moves toward the turbine rotor. It undergoes convective heat exchange with the rotor, raising its temperature and creating a temperature gradient. The cooling structure in the aero-engine is designed to reduce the rotor's temperature. Additionally, the thermal resistance at rough contact interfaces causes a temperature jump in the heat transfer between different structures of the assembled rotor. The heat transfer between the gas and the turbine disk, as well as the heat conduction in the assembled structure, directly influence the rotor's temperature distribution.

An equivalent heat transfer rotor is established based on the turbine rotor's structural and design parameters, as shown in Fig. 6. In this process of equivalence, key parameters such as mass, moment of inertia, natural frequency, and vibration modes are kept consistent. This structure comprises multiple heat exchange surfaces on the cooling and hot surfaces, as well as two bolted contact interfaces identified as ① and ②.

3.2. Heat transfer boundary conditions for hot surfaces

3.2.1. Environmental temperature boundary

The gas sequentially undergoes the thermal processes of compression, combustion, primary expansion, and secondary expansion in the core components of the T700 turboshaft engine. Based on the ideal gas Brayton cycle process, we assume that the thermal processes in compressors, gas turbines, and power turbines are isentropic, and that the combustion process is isobaric. Fig. 7 presents the known and unknown calculation parameters. The inlet airflow temperature T_1, pressure P_1, compressor pressure ratio π_c, and temperature in front of the turbine T_3 are known.

The following is the process for calculating unknown temperature and pressure.

Compression process ①−②: The pressurization process of airflow from the turboshaft engine inlet to the compressor outlet is typically simplified as the adiabatic compression process of an ideal gas. The adiabatic compression ratio, the isentropic process temperature-pressure relationship, and the steady flow energy equation are expressed as follows:

$$\begin{cases} \pi_c = \frac{P_2}{P_1} = 15 \\ T_2 = T_1\left(\frac{P_2}{P_1}\right)^{\frac{\gamma-1}{\gamma}} \\ W_c = C_P(T_2 - T_1) \end{cases} \tag{14}$$

where P_2 and T_2 represent the outlet pressure and temperature of the compressor, respectively. W_c denotes the compression work, γ is the specific heat capacity ratio (γ=1.354), and C_P is the constant pressure specific heat capacity. The calculation results are $P_2 = 1515$kPa, $T_2 = 587$K, $W_c = -328$kJ/kg.

Combustion process ②−③: Since the combustion process occurs at constant pressure, $P = 1515$ kPa. According to the steady flow energy equation, the heat energy absorbed by the combustion process is

$$q_H = C_P(T_3 - T_2) = 754 \text{ kJ/kg} \tag{15}$$

Primary expansion ③−④: The steady flow energy equation and the

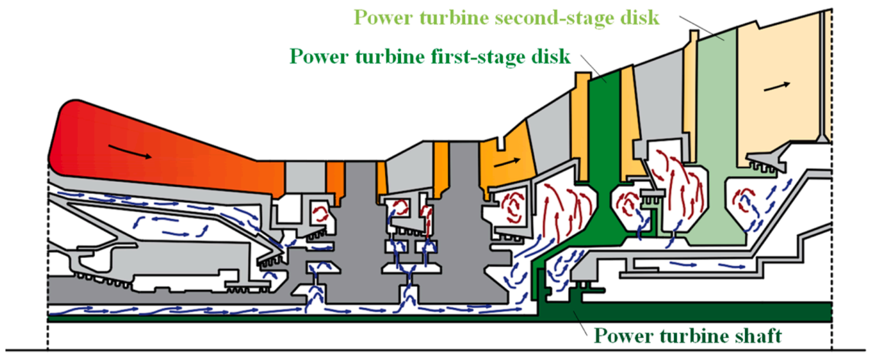

Fig. 5. Power turbine rotor of T700 turboshaft aero-engine.

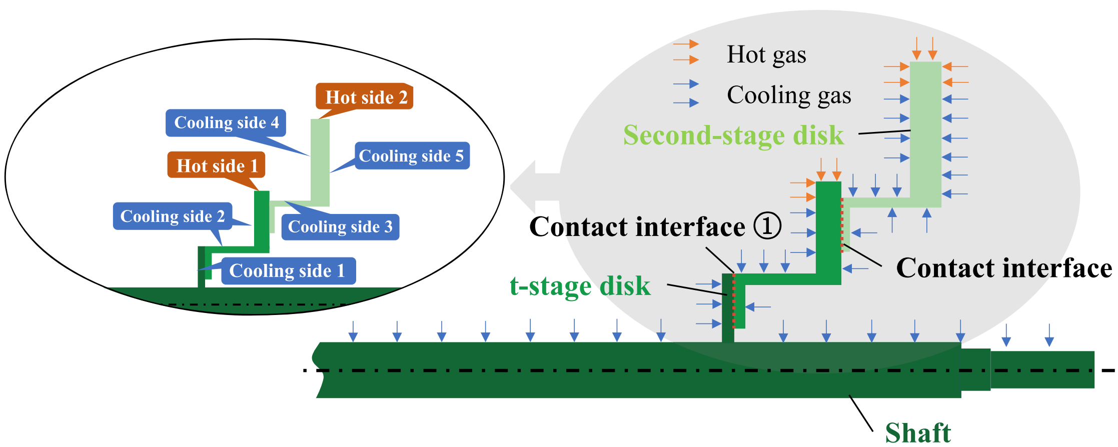

Fig. 6. The equivalent heat transfer rotor.

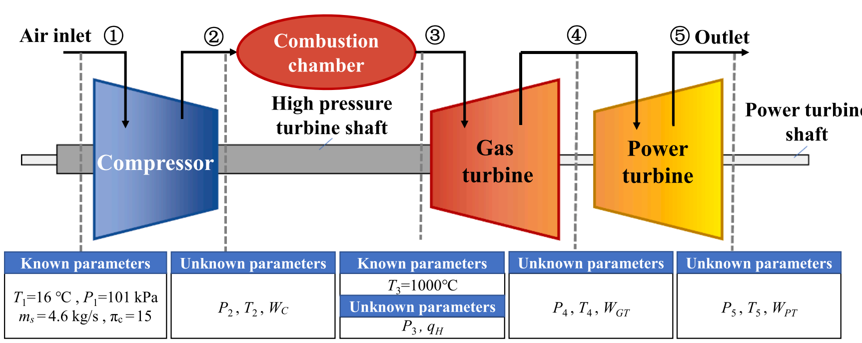

Fig. 7. Calculation parameter.

temperature-pressure relationship of the isentropic process are expressed as:

$$\begin{cases} W_{GT} = -W_c = -C_P(T_4 - T_3) \\ P_4 = P_3\left(\dfrac{T_4}{T_3}\right)^{\frac{\gamma-1}{\gamma}} \end{cases} \tag{16}$$

where W_{GT} is the work value of the primary expansion. The results for the temperature and pressure at this procession outlet are T_4 =975K, P_4 =546kPa.

Secondary expansion ④−⑤: The isentropic process temperature-pressure relationship and steady flow energy equation are written as:

$$\begin{cases} T_5 = T_4\left(\dfrac{P_5}{P_4}\right)^{\frac{\gamma-1}{\gamma}} \\ W_{PT} = -C_P(T_5 - T_4) \\ \dot{W}_{PT} = m_s W_{PT} \end{cases} \tag{17}$$

where P_5 and T_5 represent the outlet pressure and temperature of the secondary expansion, P_5 is atmospheric pressure, W_{PT} denotes the work of the secondary expansion, $\dot{W}_{PT}$ represents the output power of the power turbine, and the gas flow rate is m_s=4.6kg/s. Consequently, the results obtained are T_5=627 K, P_5=101 kPa, W_{PT}=382kJ/kg, $\dot{W}_{PT}$=1.76MW (2360 hp). Fig. 8 depicts the *P-V* and *T-s* diagrams of the

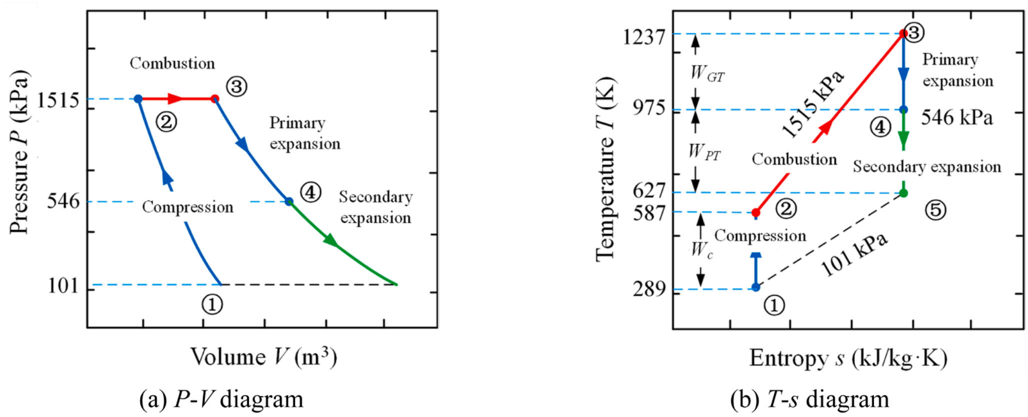

Fig. 8. Thermodynamic process.

aforementioned four processes, which provide the input boundary conditions for subsequent calculations.

The secondary expansion occurs at the turbine disk position of the power turbine rotor, leading to the following expression for the hot end gas temperature and pressure along the axial direction:

$$\begin{cases} T = -1912.08Z + 975 \\ P = 2445.06Z + 546 \end{cases}, \ Z \in [0, 0.182]\text{m} \tag{18}$$

where Z represents the axial coordinate starting from the front of the first stage turbine disk of the power turbine rotor.

3.2.2. Convection heat transfer coefficient boundary

The convective heat transfer coefficient on hot side surfaces is determined based on the temperature and pressure distributions of the fluid medium in the vicinity of the power turbine rotor's hot side.

$$h_{heat} = \left(\frac{2r_0}{0.57}\right)^{0.8}\left(\frac{\Omega}{3000}\right)^{0.8}\left[100 + (100P(Z) - 1)\left(1.3\times10^{-4}T^2(Z) - 0.2T(Z) + 147.3\right)\right] \tag{19}$$

where r_0 is the radius of the disk edge, and Ω denotes the rotational speed of the rotor. This equation is applicable when $P \in [100, 2000]$kPa. For the hot surface of the first-order disk, r_0=0.085 m, Z∈[0.05,0.06]m. For the second-order disk, r_0=0.09 m, Z∈[0.095,0.108]m. Substituting the above radius and axial coordinates into Eq. (18), the convective heat transfer coefficient at the hot end surfaces can be determined for a given rotational speed.

Fig. 9 illustrates the variation of the convective heat transfer coefficient on the hot side of the first- and second-stage turbine disks with axial position and rotational speed. As the high-temperature gas passes through the first and second turbine disks, both pressure and temperature gradually decrease, leading to a reduction in the heat transfer coefficient. Moreover, an increase in rotational speed enhances the heat exchange efficiency between the hot surface and the gas.

3.3. Heat transfer boundary conditions for cooling surfaces

The cooling gas primarily undergoes convection heat exchange with the disk side. The cooling structure design impacts the heat exchange efficiency between the disk side and the cooling medium. Aero-engine rotor disk cooling structures typically consist of several types. These include a free disk structure, a stator-rotor structure without external air supply, an open/closed stator-rotor structure with air supply, and a dual rotor design with different flow patterns. These structures are illustrated in Fig. 10.

The first-stage disk, the second-stage disk and the sealing structure of the T700 power turbine together form five cavities, as shown in Fig. 11. Cavities II, III, and IV are closed stator-rotor structures with air supply, and cavity I and V feature open stator-rotor structures with air supply.

Owen et al. [15] conducted experiments on an open stator-rotor with air supply (Fig. 10(c)), obtaining the average convection heat transfer coefficient on the disk side as follows:

$$h_{exo-ave} = \begin{cases} 0.0145\mu {r_d}^{-1}\left(\dfrac{C_w}{G}\right)^{4/5}, Re \leq 10^5 \\ \mu {r_d}^{-1}\left\{\left[0.0145\left(\dfrac{C_w}{G}\right)^{4/5}\right]^6 + \left[0.0171\left(1+\dfrac{11C_w{r_d}^2}{50Re{r_{in}}^2}\right)Re^{0.814}\right]^6\right\}^{1/6}, 10^5 < Re \leq 10^6 \\ 0.0197\mu Re^{4/5}{P_r}^{3/5}{r_d}^{-1}(2.6+m)^{-4/5}(2+m)\left(1+\dfrac{11C_w{r_d}^2}{50Re{r_{in}}^2}\right), Re > 10^6 \end{cases} \tag{20}$$

where r_{in} represents the inlet gap radius difference, r_d denotes the disk radius, C_w is the inlet flow coefficient, Re stands for the rotational

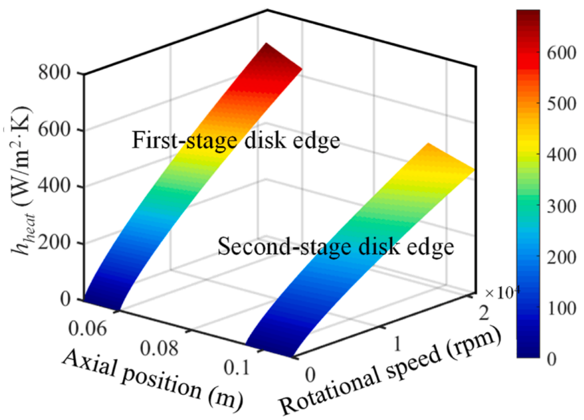

Fig. 9. The convective heat transfer coefficient with axial position and rotational speed (r_0=0.1 m).

Reynolds number, μ is the thermal conductivity of the medium (μ=0.23 W·m^{-1}·K^{-1}), G is the gap ratio (It is defined as $G=S/r_d$, where S is the axial clearance between rotor and stator), and P_r is Prandtl number. The aforementioned experimental relationship is applicable to $Re\in[0,4\times10^6]$, $G\in[0.01,0.18]$, $C_w\in[1.4\times10^4, 9.8\times10^5]$, r_d/r_{in}=7.5, with air serving as the cooling medium. The sealing structure (Fig. 10(d)) is typically designed to prevent gas backflow. Owen et al. obtained the expression for the average convection heat transfer coefficient of the disk side temperature with a parabolic distribution of this structure as follows:

$$h_{exc-ave}=\frac{\mu r_d{}^{-1}Re}{\pi}\left[C_m(r_d,S_{out})+\left(\frac{r_s}{r_d}\right)^5(C_m(r_s,S)-C_m(r_s,S_{out}))\right] \tag{21}$$

where S_{out} represents the air flow outlet gap, and r_s is the maximum radius of the gap. The expression of the coefficient C_m is:

$$C_m(r,s)=\left\{\left[0.0553Re^{-1}\left(\frac{rC_w}{s}\right)^{4/5}\right]^6+\left[0.0655Re^{-0.186}\left(\frac{11C_wr^2}{50Rer_{in}{}^2}+1\right)\right]^6\right\}^{1/6} \tag{22}$$

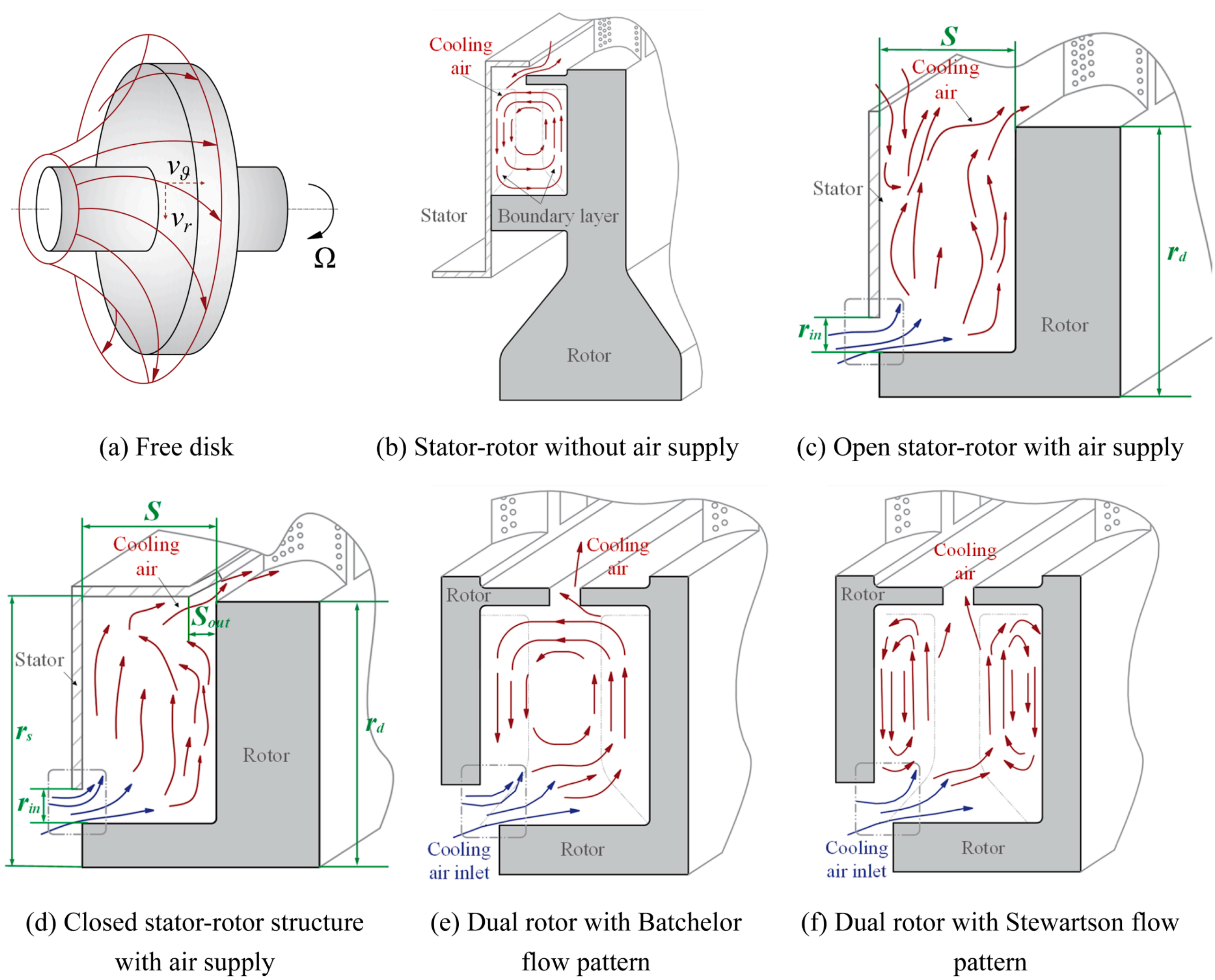

Fig. 10. The cooling structure of the aero-engine.

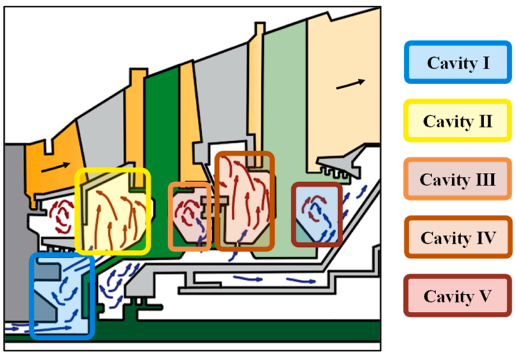

Fig. 11. Five cavities for cooling.

Figs. 12 and 13 illustrate the variations of the average convective heat transfer coefficient with Re, G, and C_w for the open and closed structures with air supply. It is observed that the average convection heat transfer coefficient increases nearly linearly as the Re and C_w increase near the cooling side disk surface. In the open structure, as the G uniformly increases, the equivalent heat transfer coefficient decreases. Particularly, for $G \leq 0.03$, the equivalent heat transfer coefficient shows high sensitivity to changes in G, while for $G > 0.03$, the sensitivity of the equivalent heat transfer coefficient to G diminishes. This information provides guidance for robust design.

Table 1 presents the design and operating parameters used for calculating the convective heat transfer coefficient of each cooling side surface.

Table 1
Parameters used to calculate cooling side surfaces convection heat transfer coefficient.

Parameters	Cavity I	Cavity V	
Inlet flow coefficient C_w	6.4×10^4	6.4×10^4	
Gap ratio G	0.5	0.3	
Disk radius r_d	0.085 m	0.09 m	
Parameters	Cavity II	Cavity III	Cavity IV
Inlet flow coefficient C_w	3×10^4	1×10^4	2×10^4
Maximum radius of the gap r_s	0.081 m	0.069 m	0.069 m
Disk radius r_d	0.085 m	0.085 m	0.09 m

3.4. Contact interface boundary conditions

The power turbine rotor of the T700 turboshaft engine features two contact interfaces assembled by bolts, as shown in Fig. 14. Table 2 lists the structural and material parameters utilized to calculate the structural-structural heat transfer characteristics. Aside from the fractal dimension, fractal roughness, and RMS height, which are derived from experimental data, other parameters are obtained from material properties, rotor structure, or empirical equations.

M6 bolts of grade 5.6 are utilized for assembling the substructure, with a standard tightening torque of 4.8 N·m. Consequently, this study employs a maximum tightening torque of 5 N·m for subsequent

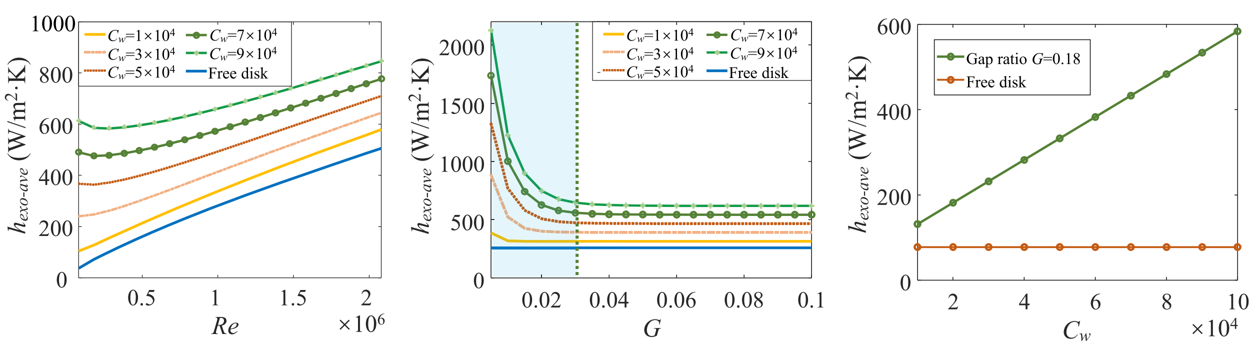

(a) Rotational Reynolds number (b) Gap ratio (c) Inlet flow coefficient

Fig. 12. The average convection heat transfer coefficient in an open structure with air supply.

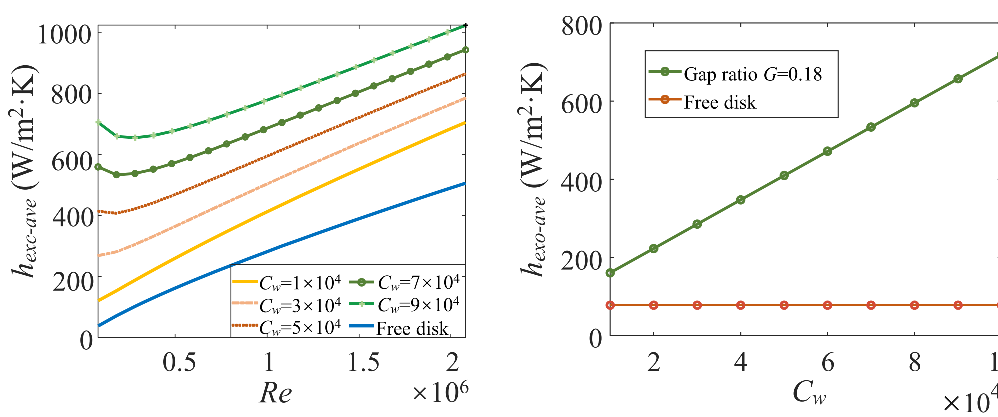

(a) Rotational Reynolds number (b) Inlet flow coefficient

Fig. 13. The average convection heat transfer coefficient in a closed structure with air supply.

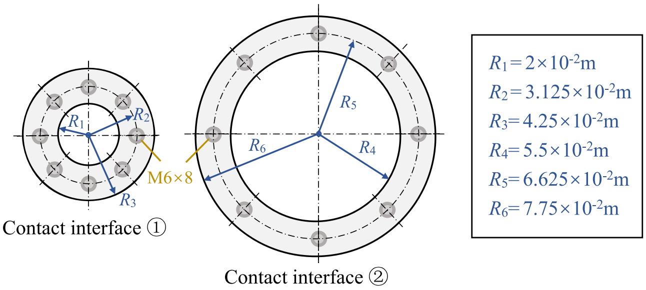

Fig. 14. Contact interfaces.

Table 2
Structural and material parameters of two contact interfaces.

Parameters	Value	Parameters	Value
Fractal dimension D_f of interfaces	1.6182	RMS height σ	1.56×10^{-6}
Fractal roughness G_f of interfaces	4.1252×10^{-7}	Small probability value P_s	0.05
Equivalent hardness $\widetilde{H}$	2.04GPa	Nominal contact area of interface ①	4.4×10^{-3} m^2
Equivalent elastic modulus $\widetilde{E}$	108GPa	Nominal contact area of interface ②	0.011 m^2
Bolts number N_{bolt} of interfaces	8	Thermal Conductivity k_a,k_b	50 W/m·K
Bolt hole inner diameter d	0.006 m	Bolt hole diameter coefficient α	1.125

research. The relationship between the preload torque M_b and bolt preload force F is approximately expressed as $F = 5M_b/d$. By substituting the bolt preload into Eqs. (8)–(12), the equivalent TCC of interface ①/② under different assembly parameters is calculated (as shown in Table 3). This provides essential interface boundary conditions for analyzing structural-structural heat transfer characteristics.

4. Influence of operating parameters related to working condition

The environmental-structural-structural heat transfer characteristics are significantly influenced by operating parameters related to working conditions, particularly rotational speed and rotational Reynolds number. For aeroengine turbine rotors operating under low Mach number conditions, these parameters are crucial in governing the convective heat transfer between the fluid medium and the rotor structure's surface. Consequently, this section initially examines the impact of rotational speed and rotational Reynolds number on environmental-structural-structural heat transfer characteristics using an equivalent heat transfer model.

4.1. Different rotational speeds

The heat transfer coefficients for the first-stage and second-stage disk edges, as well as the cooling surfaces, are calculated over a range of rotational speeds from 0 to 21,000 rpm. This analysis considers the maximum rotational speed of the T700 power turbine rotor, which is 20,900 rpm. The results are summarized in Table 4.

Table 4
Heat transfer coefficients at different rotational speeds.

Rotational speed (rpm)	First-stage disk edge (W/(m^2·K))	Second-stage disk edge (W/(m^2·K))	Cooling surface (W/(m^2·K))
0	0	0	Cooling surface 1:
1000	59.82	40.30	133.0
2000	104.16	70.17	Cooling surface 2:
3000	144.08	97.05	125.4
6000	250.86	168.99	Cooling surface 3
9000	346.98	233.74	:114.0
12,000	407.40	274.44	Cooling surface 4:
15,000	522.14	351.73	108.3
18,000	604.13	406.96	Cooling surface 5:
21,000	683.42	460.38	67.93

The environmental-structural-structural heat transfer characteristics under different rotational speeds are analyzed using the above boundary conditions. Fig. 15 illustrates the temperature distribution along two radial paths of the power turbine at various ω. The observations are as follows:

(1) The temperature of the first-stage turbine disk increases nearly linearly along the radial direction (Path I). In contrast, the temperature of the second-stage turbine disk rises non-linearly along the radial direction (Path II), peaking near the disk's edge.
(2) The disk temperature remains at room temperature when the rotor is stationary. The efficiency of heat exchange between the high-temperature gas and the disk edge improves as the speed increases, leading to an elevation of the turbine disk temperature. However, beyond 6000 rpm, the rate of temperature rise diminishes gradually, suggesting a reduced impact of rotational speed on the temperature distribution.

Fig. 16 illustrates the temperature distribution along two axial paths of the turbine rotor at various rotation speeds. The following observations can be made:

(1) The temperature along Path III shows a gradual increase, with higher temperatures observed near the turbine disk edge. This is attributed to Path III's proximity to cavity ① and the first-stage turbine disk. Path IV, between the first- and second-stage disks, exhibits temperatures peaking near the first-stage disk and decreasing axially.
(2) Heat transfer efficiency increases with higher rotational speeds, resulting in higher temperatures along Paths III and IV, especially near the first-stage disk edge. Above 6000 rpm, the temperature increment decreases, indicating a temperature low-sensitivity zone to rotational speed. The critical speed for the power turbine rotor is approximately 6000 rpm.

The critical rotational speed threshold correlates with the transition in fluid dynamics. The transition from laminar to turbulent flow escalates as rotational speed rises, significantly impacting heat transfer efficiency. Upon reaching a critical speed, turbulent flow stabilizes, diminishing the influence of rotational speed on heat transfer efficiency.

Table 3
The equivalent TCC under different assembly parameters.

Tightening torque (N·m)	Equivalent TCC of interface ① (W/m^2·K)	Equivalent TCC of interface ② (W/m^2·K)	Tightening torque (N·m)	Equivalent TCC of interface ① (W/m^2·K)	Equivalent TCC of interface ② (W/m^2·K)
0.05	175.8	82.9	2	10,174	4799.1
0.1	1329.5	627.1	3	13,568	6400.1
0.5	3918.9	1848.5	4	16,707	7880.9
1	6286.4	2965.6	5	19,689	9287.1

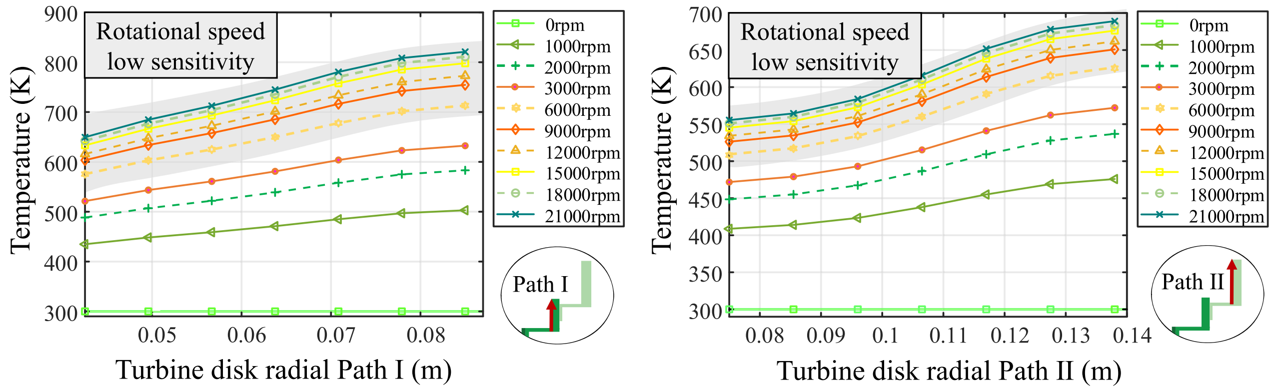

(a) Path I (b) Path II

Fig. 15. Temperature distribution of Path I and Path II under different rotational speeds.

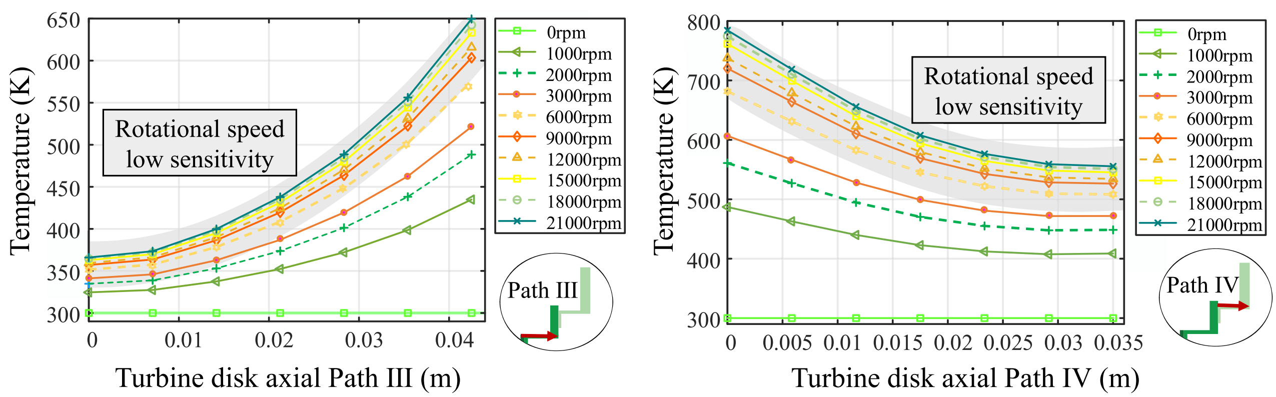

(a) Path III (b) Path IV

Fig. 16. Temperature distribution of Path III and Path IV under different rotation speeds.

Table 5
Heat transfer coefficients at different rotational Reynolds numbers.

Rotational Reynolds numbers $\times 10^4$	Cooling surface 1 W/(m^2·K)	Cooling surface 2 W/(m^2·K)	Cooling surface 3 W/(m^2·K)	Cooling surface 4 W/(m^2·K)	Cooling surface 5 W/(m^2·K)	First-stage disk edge W/(m^2·K)	Second-stage disk edge W/(m^2·K)
9	54.9	40.7	25.8	24.4	67.93	360	252
12	64.9	53.3	40.7	38.4	67.93	360	252
15	76.4	67.3	53.3	47.2	67.93	360	252
18	88.10	79.7	67.3	63.6	67.93	360	252
21	99.6	91.7	79.7	75.3	67.93	360	252
24	110.7	103	91.7	86.6	67.93	360	252
27	122.3	114	103	97.6	67.93	360	252
30	133.0	125.4	114	108.3	67.93	360	252

This phenomenon is also associated with boundary layer thickness. Convection heat transfer mainly occurs in the boundary layer region. At lower rotational speeds, the boundary layer thickness is highly responsive to rotational speed changes, making heat transfer more sensitive. However, at higher speeds, the boundary layer becomes sufficiently thin, reducing the sensitivity of heat transfer to variations in rotational speed. The centrifugal force also influences this process. As rotational speed rises, the increasing centrifugal force drives faster gas flow across the rotor surface, promoting enhanced heat transfer. However, at higher rotational speeds, the effect of centrifugal force stabilizes, leading to a steady-state heat transfer effect.

4.2. *Different rotational Reynolds numbers*

The rotational Reynolds number is a dimensionless number that describes the flow characteristics of fluids in a rotating system. It is defined as:

$$Re = \frac{\omega R^2}{\nu} \tag{23}$$

where R is the rotor radius, ω is the angular velocity, and ν is the kinematic viscosity of the fluid medium. This section delves into the environmental-structural-structural heat transfer characteristics of the power turbine rotor under different rotational Reynolds numbers.

Table 5 displays the calculated average convective heat transfer coefficients for the cooling and hot surfaces during steady operation at

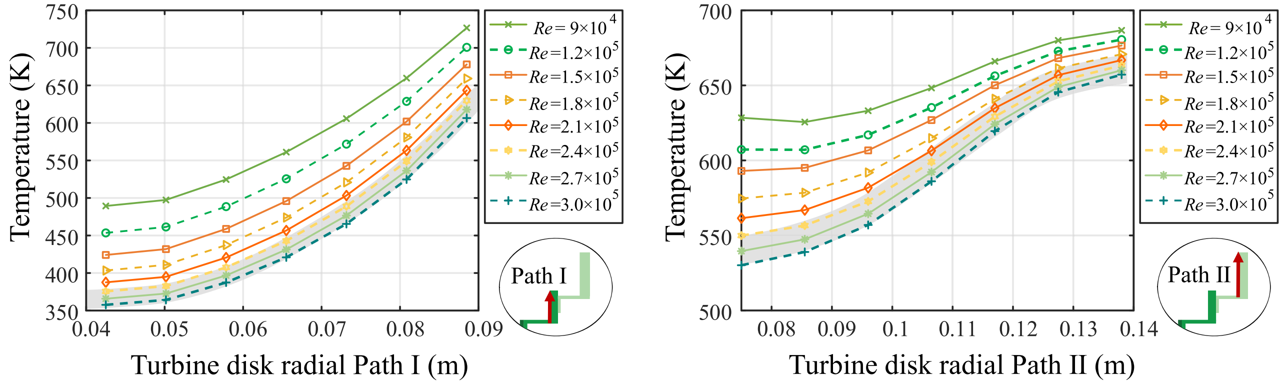

(a)Path I (b) Path II

Fig. 17. Temperature distribution of Path I and Path II under different Reynolds numbers.

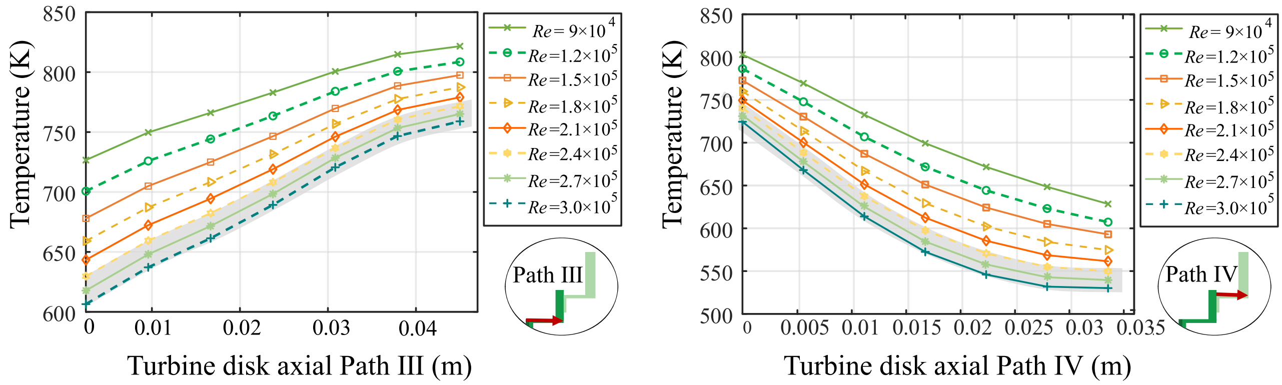

(a) Path III (b) Path IV

Fig. 18. Temperature distribution of Path III and Path IV under different Reynolds numbers.

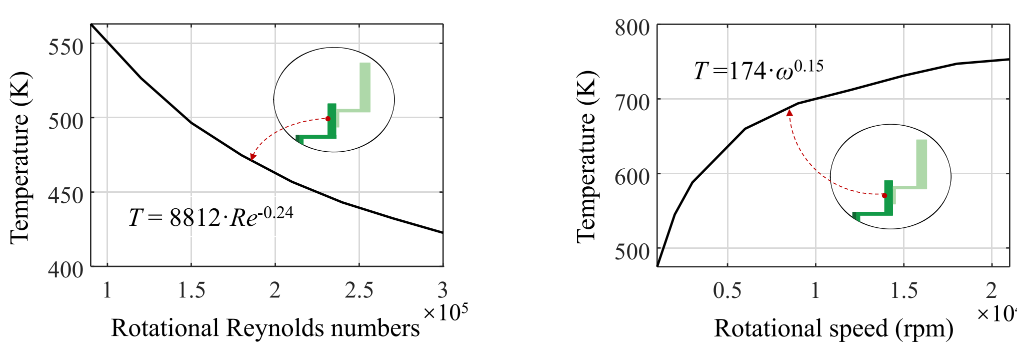

(a) Rotational Reynolds numbers (b) Rotational speed

Fig. 19. The relationship between the rotational Reynolds number/rotational speed and temperature.

10,000 rpm, with the cooling surface's rotational Reynolds number spanning from 9×10^4 to 3×10^5.

The environmental-structural-structural heat transfer characteristics under different rotational Reynolds numbers are analyzed using the above boundary conditions, as shown in Fig. 17. It is observed that the temperature of both the first- and second-stage turbine disks increases along the radial direction, peaking near the disk edge. As the rotational Reynolds number increases, the heat exchange efficiency between the cooling gas and the turbine disk improves, resulting in a reduction in the overall temperature of the turbine disk. This cooling effect is more pronounced closer to the root of the turbine disk. Beyond a rotating Reynolds number of 2.4×10^5, the rate of temperature increase on the disk decreases significantly, indicating a diminishing impact of the rotating Reynolds number on the temperature field.

Fig. 18 shows the temperature distribution along two axial paths at various rotational Reynolds numbers. The temperature increases gradually along the axial position of Path III and decreases gradually along Path IV. The rate of temperature increase slows as one approaches the first-stage disk edge. Furthermore, an increase in the rotational Reynolds number results in a decrease in the overall turbine temperature. For the

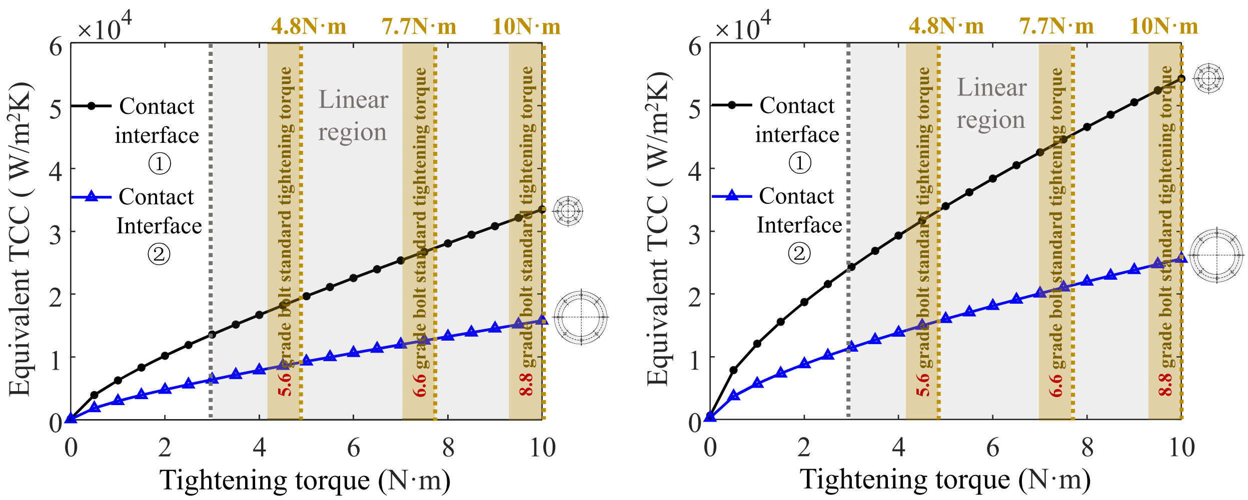

(a) D_f=1.4041, G_f=6.8×10^{-10} (b) D_f=1.6182, G_f=4.1252×10^{-7}

Fig. 20. Equivalent TCC under different assembly mechanical parameters.

power turbine rotor of the T700 turboshaft engine, the sensitivity of the temperature field to the *Re* gradually decreases when *Re* exceeds a certain critical value.

At low rotational Reynolds numbers, the transition from laminar to turbulent flow, changes in boundary layer thickness, and enhanced rotational effects result in a high sensitivity of the convective heat transfer coefficient to changes in the Reynolds number. As the Reynolds number increases, these effects stabilize, reducing their influence on heat transfer at higher Reynolds numbers.

Fig. 19 shows the quantitative relationship between the rotational Reynolds number/rotational speed and temperature along Path I. Quantitative analysis reveals an exponential correlation between the rotational Reynolds number/rotational speed and temperature.

5. Influence of interface contact parameters associated with assembly

Given that the heat transfer paths in power turbine rotor are typically formed by bolted connections, the environmental-structural-structural heat transfer characteristics are influenced by interface contact parameters related to assembly. This section initially examines the impact of assembly mechanical parameters, structural design parameters, and surface topography parameters on the equivalent TCC. Subsequently, a finite element model of the assembled rotor is employed to investigate the environmental-structural-structural heat transfer characteristics under varying assembly parameters.

5.1. Influence of multiple factors on equivalent TCC

5.1.1. Assembly mechanical parameters

Variations in tightening torque impact the actual contact area of the connection interface, thereby influencing the TCC. Fig. 20 illustrates the equivalent TCC of interface ①/② under varying assembly tightening torques. The analysis presents results considering two distinct surface morphologies to ensure the reliability of the conclusions. Several intriguing findings emerge:

(1) The equivalent TCC increases as tightening torque increases. This phenomenon is attributed to the increase in tightening torque, which results in greater contact pressure at the rough surfaces. As the pressure rises, the actual contact area between the interfaces enlarges. Eqs. (8) and (9) demonstrate that this reduces the contact thermal resistance (enhances contact thermal

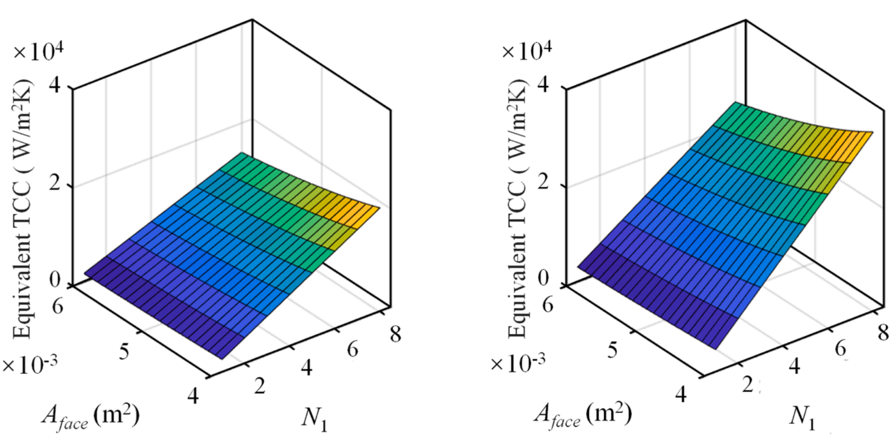

(a) D_f=1.4041, G_f=6.8×10^{-10} (b) D_f=1.6182, G_f=4.1252×10^{-7}

Fig. 21. Equivalent TCC of interface ① under different structural design parameters.

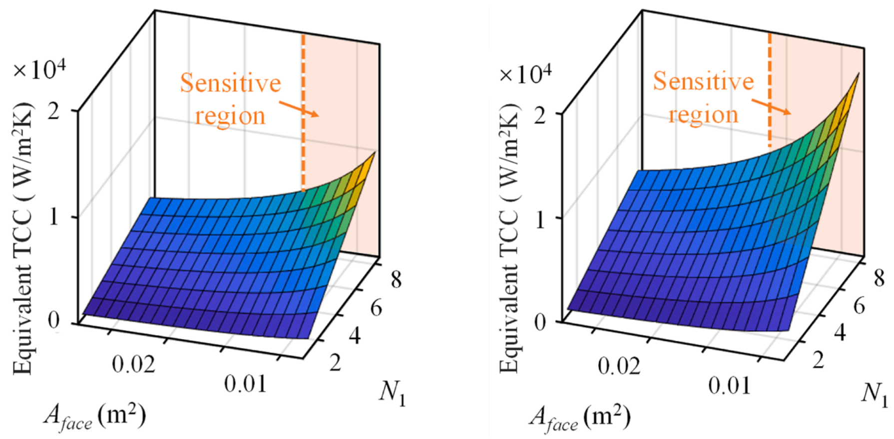

Fig. 22. Equivalent TCC of interface ② under different structural design parameters.

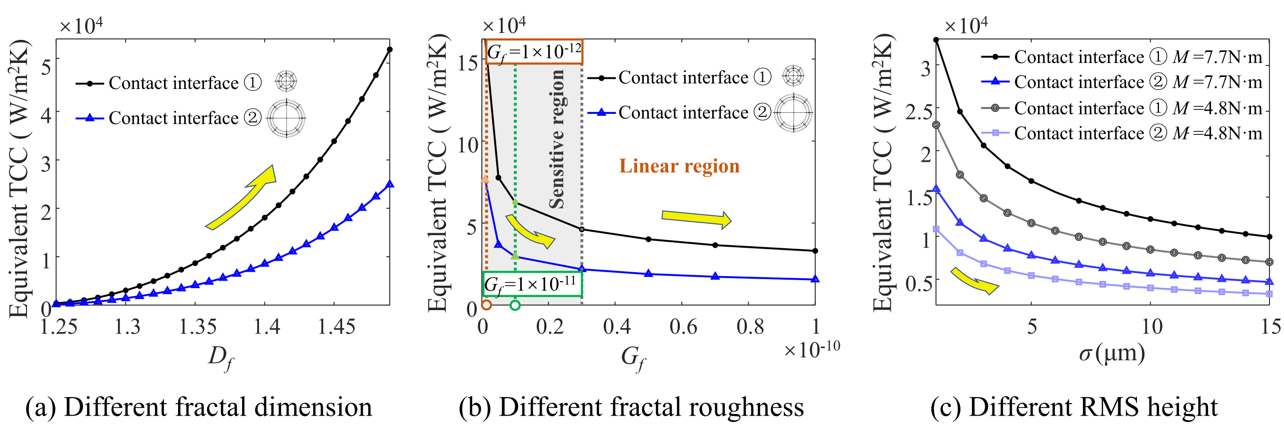

Fig. 23. Equivalent TCC under different surface topography parameters.

conductivity), thus diminishing the interface's capacity to resist heat transfer.

(2) The standard tightening torques for M6 bolts of grades 5.6, 6.6, and 8.8 are 4.8 N·m, 7.7 N·m, and 10 N·m, respectively. The equivalent TCC demonstrates near-linear behavior at these standard tightening torques.

(3) Furthermore, for the identical type of bolt, quantities, and tightening torques, the equivalent TCC at interface ① exceeds that at interface ② significantly. This disparity suggests that smaller interfaces exhibit lower contact thermal resistance, which can be attributed to their ability to achieve more complete contact under the same parameters.

5.1.2. Structural design parameters

Structural design parameters, such as the apparent contact area of the interface and the number of bolts, significantly impact the heat transfer characteristics of the power turbine rotor. Fig. 21 and Fig. 22 depict the impact of these parameters on the equivalent TCC of interface ① and interface ②, respectively. The results indicate that as the number of circumferential bolts increases, the equivalent TCC exhibits a nearly linear increase. Furthermore, this effect is more pronounced with a smaller apparent contact area. Conversely, an increase in the apparent contact area results in a decrease in the equivalent TCC. Notably, for a larger interface, an insufficient apparent contact area may lead to contact heat conduction entering the sensitive area.

5.1.3. Surface topography parameters

Interfaces with different morphologies exhibit diverse interface dynamic characteristics under the identical preload load, thereby impacting the heat transfer characteristics between interfaces. Fig. 23 illustrates the influence of fractal dimension, fractal roughness, and RMS height of the interface on the equivalent TCC of the two interfaces. Fig. 23(a) shows that the equivalent TCC gradually increases with the fractal dimension. Fig. 23(b) indicates a sudden drop phenomenon as the fractal roughness increases. For fractal roughness values below 3×10^{-11}, there is a sensitive region where the equivalent TCC is highly sensitive to fractal roughness. Beyond this threshold, the equivalent TCC decreases nearly linearly, with significantly reduced sensitivity. Fig. 23 (c) shows that as the surface RMS height increases, the equivalent TCC of the two interfaces decreases, with a diminishing rate of decrease.

5.2. Heat transfer characteristics with different assembly parameters

Changes in TCC ultimately manifest as changes in the temperature field of the combined rotor. To investigate the heat transfer characteristics under different TCCs, the local temperature field distribution characteristics at the interface and the quantitative temperature distribution along the critical path are analyzed. Fig. 24 shows the local environmental-structural-structural temperature distribution characteristics of the interface under various assembly parameters. It is observed that smaller tightening torques result in a more pronounced temperature field jump phenomenon at the interface. Conversely, increasing tightening torque enhances the continuity of temperature

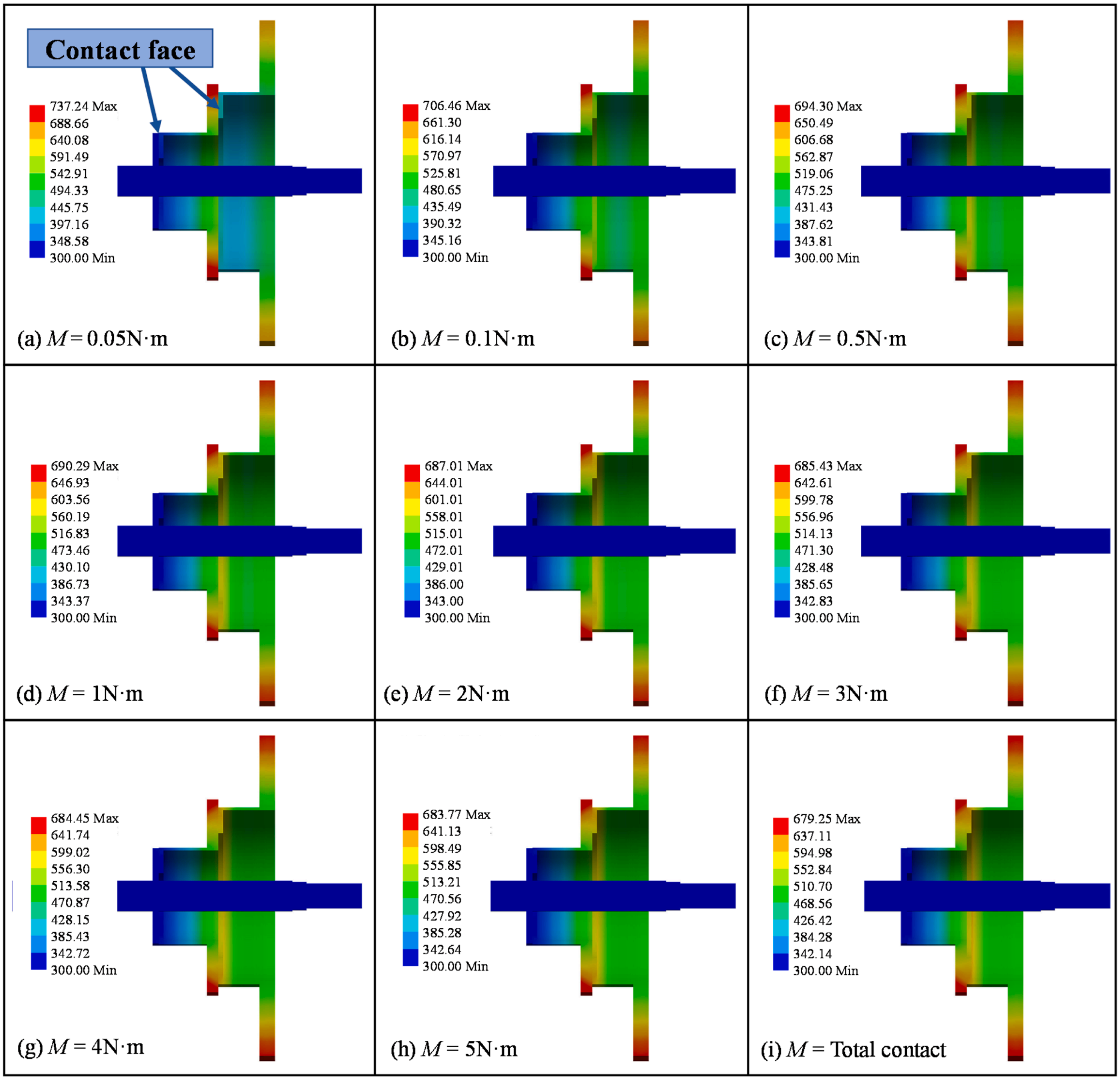

Fig. 24. The local environmental-structural-structural temperature under different assembly parameters.

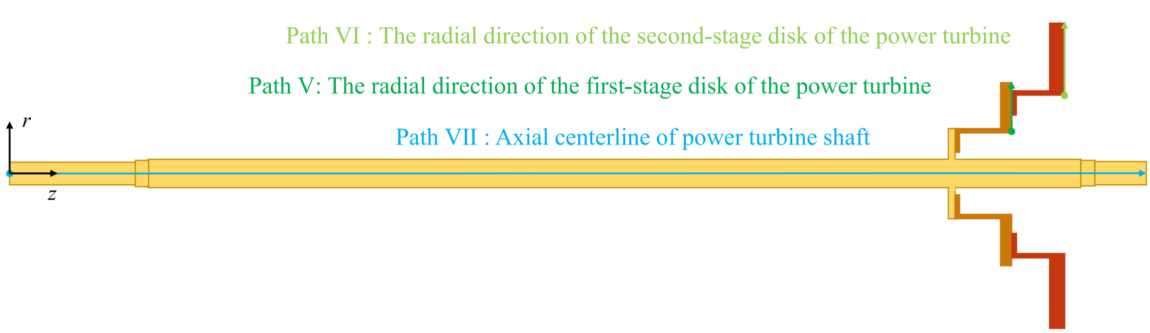

Fig. 25. Three paths for quantitative temperature analysis.

transfer along the axial direction at the interface. This is attributed to the increased actual contact area of the interface at higher tightening torques, leading to a higher equivalent TCC.

Fig. 25 shows the quantitative description of the environmental-structural-structural heat transfer characteristics along three paths. Paths V and VI represent radial paths, while Path VII is an axial path.

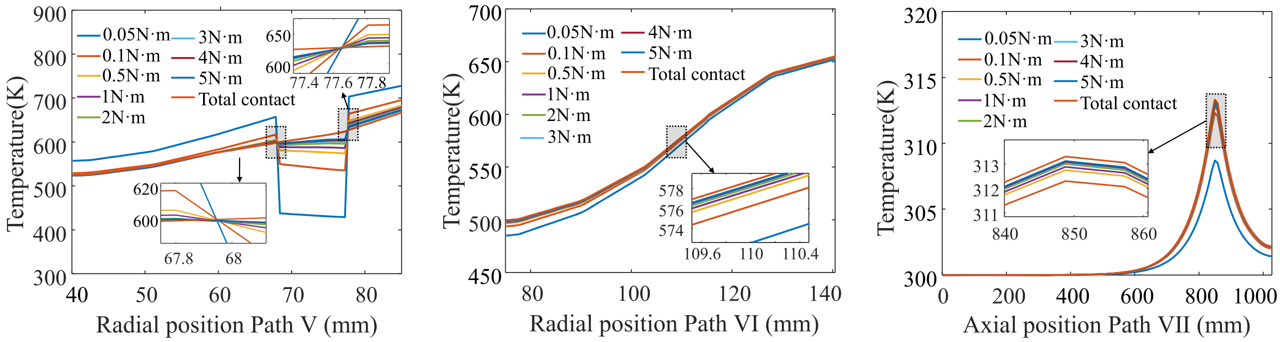

(a) Path V (b) Path VI (c) Path VII

Fig. 26. Environmental-structural-structural temperature distribution along three paths.

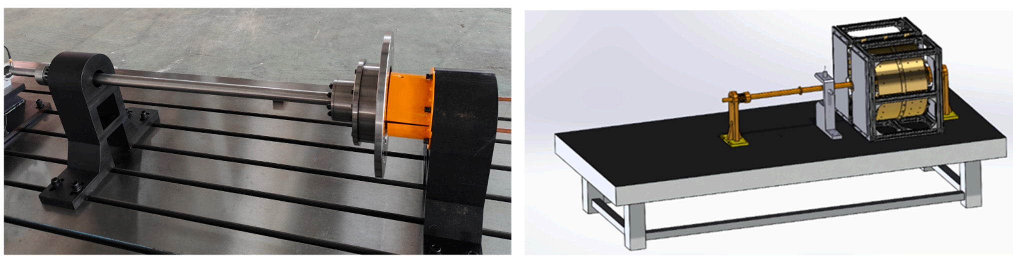

(a) The assembly rotor (b) The heating structure

Fig. 27. Experiment setup.

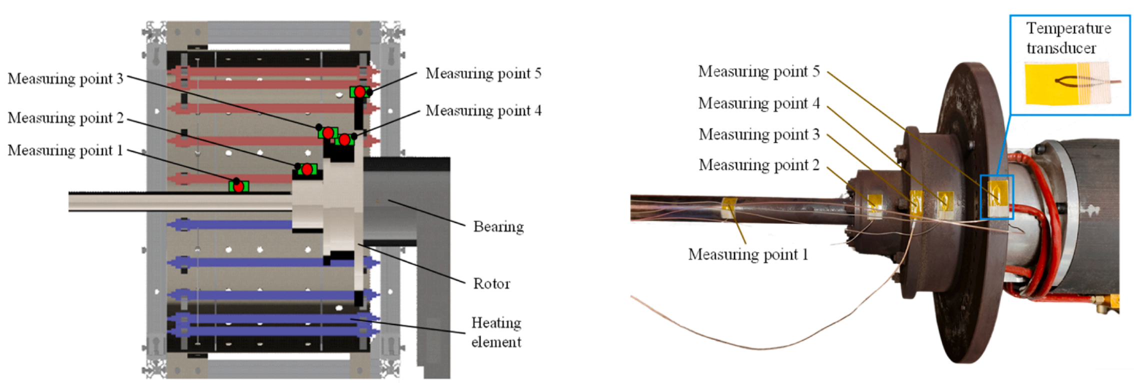

(a) Diagram of heated area and measuring point (b) The actual layout of sensors

Fig. 28. Heated area and measuring point location.

Given that the power turbine rotor emphasizes the shaft's bending mode, even small temperature changes on the shaft can significantly impact its bending dynamic behavior. Thus, a quantitative description of the temperature distribution along Path VII is essential.

Fig. 26(a) depicts the environmental-structural-structural temperature distribution along Path V, where a temperature jump occurs across the two interfaces. This jump diminishes gradually with increasing tightening torque, becoming negligible at the standard torque of 4.8 N·m for grade 6.6 bolts. At full contact, the radial temperature remains continuous. The temperature distribution along Path VI (Fig. 26(b)) reveals that under this boundary condition, the radial temperature difference decreases as the tightening torque increases, eventually approaching the temperature distribution at full contact. Fig. 26(c) illustrates the temperature distribution along Path VII, indicating that as the tightening torque increases, the temperature difference along the axial direction gradually rises. The reason is that reduced heat transfer resistance facilitates greater heat transfer from the turbine disk to the shaft. In addition, a critical threshold of assembly parameter can be clearly found in Fig. 26(a), which is about 0.5 N·m. When it is less than this value, there is a large temperature jump on the heat transfer path. This means that the rotor cannot effectively transfer heat to the cooling area, resulting in local overheating.

6. Experiment verification

In this Section, the reliability of the model is verified. Fig. 27 shows the experiment setup of the assembly rotor and heating structure. The rotor consists of three substructures, assembled by bolts, forming two rough contact surfaces.

As shown in Fig. 28, the turbine disk is locally heated, and five

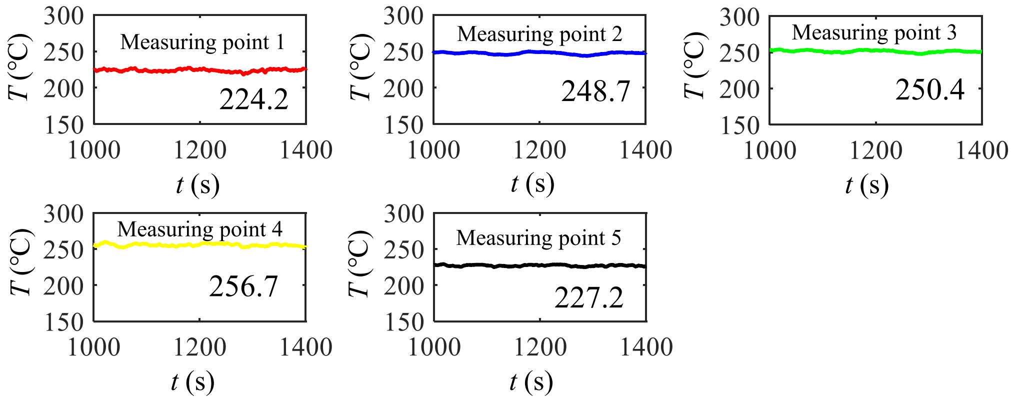

Fig. 29. Temperature at five measuring points.

Table 6
Relative error analysis of experiment results and simulation results.

	Experiment result (℃)	Simulation result (℃)	Relative error (%)
Measuring point 1	224.2	222.7	0.67
Measuring point 2	248.7	247.7	0.40
Measuring point 3	250.4	244.9	2.20
Measuring point 4	256.7	257.9	0.47
Measuring point 5	227.2	226.9	0.13

measuring points are arranged on the assembled rotor.

Fig. 29 shows the temperature measured at five measuring points after the temperature field is stabilized. It can be found that the average temperatures within 400 s from measuring point 1 to measuring point 5 are 224.2℃, 248.7℃, 250.4℃, 256.7℃, 227.2℃, respectively.

A temperature field simulation analysis under full contact is performed based on the conditions in the above experiment. The experiment results at the five measuring points are compared with the simulation results, and relative error analysis is performed, as shown in Table 6. The maximum relative error of 2.2 % confirms the robustness and practical relevance of the model used for analyzing heat transfer characteristics.

7. Conclusions

In this work, considering the combined effects of operating parameters and interface parameters, the environmental-structural-structural heat transfer characteristics of T700 turboshaft engine's power turbine rotors are systematically analyzed, and the critical thresholds of these parameters and their quantitative relationships with temperature are explored. The findings are anticipated to enhance the design and efficiency of the power turbine rotor systems in various industrial applications. The main conclusions are:

(1) An environmental-structural-structural heat transfer model is developed using fractal theory and the finite element method. This model incorporates the effects of operating parameters related to working conditions and interface contact parameters associated with assembly. Operating parameters primarily influence convective heat transfer, while interface contact parameters mainly govern heat conduction. These parameters synergistically affect the temperature of the power turbine rotor. The modeling process begins with the development of a convection heat transfer model for the substructure. The substructure is then integrated into a complete rotor model using a contact thermal resistance model that accounts for the distribution of bolt contact pressure.

(2) The heat exchange efficiency between the high-temperature gas and the hot side increases with rotational speed. In contrast, the heat exchange efficiency between the cooling gas and the cooling side is positively correlated with the rotational Reynolds number. These contributions to the turbine disk's overall temperature exhibit contrasting trends. It was found that the rotational Reynolds number and rotational speed have an exponential relationship with temperature through a quantitative analysis process. These insights are pivotal for optimizing the turbine disk's temperature distribution.

(3) Beyond a critical rotational speed of 6000 rpm or a critical rotational Reynolds number of 2.4×10^5, the temperature enters a low-sensitivity regime, indicating that the temperature in this regime is minimally affected by these factors. When operating conditions exceed critical thresholds, heat transfer performance will changes significantly, potentially leading to engine rotor overheating, which would adversely affect engine reliability and safety. This highlights the importance of accounting for these critical thresholds when designing the cooling system and analyzing the dynamic performance of thermoelastic coupling.

(4) The equivalent TCC at interfaces increases with tightening torque. Under standard tightening torque condition for M6 bolt, the equivalent TCC falls within a near-linear range. Variations in the number of bolts, apparent contact area, fractal dimension, fractal roughness, and surface RMS height lead to different trends in equivalent TCC within certain range. Furthermore, smaller interfaces exhibit less significant contact hindrance effects under identical parameters.

(5) The variation in assembly parameter influences the environmental-structural-structural heat transfer characteristics. Specially, decreasing the tightening torque reduces the actual contact area at the interface, resulting in a more pronounced temperature jump. It easily causes local overheating of the assembled power turbine rotor. It is worth noting that there is a critical threshold for assembly parameters. Identifying this critical threshold will help avoid some problems such as reduced heat transfer performance due to excessive interface thermal resistance, thereby ensuring that heat can be transferred from the high temperature area to the cooling area faster. These results underscore the importance of precise tightening protocols to stabilize thermal performance and minimize temperature gradients at critical interfaces.

CRediT authorship contribution statement

Yazheng Zhao: Writing – original draft, Validation, Data curation, Conceptualization. **Jin Zhou:** Writing – review & editing, Supervision, Funding acquisition. **Mingjie Guo:** Data curation. **Yuanping Xu:** Writing – review & editing, Supervision.

Declaration of competing interest

The authors declare that they have no known competing financial interests or personal relationships that could have appeared to influence the work reported in this paper.

Acknowledgment

This work was carried out with the support and funding allocated to the National Natural Science Foundation of China (No. 52075239).

Appendix A

The interpolation functions in the shape function matrix are expressed as:

$$\begin{cases} N_i = \dfrac{1}{2\Delta}(a_i + b_i r + c_i z) \\ N_j = \dfrac{1}{2\Delta}(a_j + b_j r + c_j z) \\ N_m = \dfrac{1}{2\Delta}(a_m + b_m r + c_m z) \end{cases} \tag{A1}$$

where the unknown parameter Δ is equal to $b_i c_j + b_j c_i$. The coefficients $a_i, b_i,\ c_i, a_j, b_j, c_j, a_m, b_m,\ c_m$ are undetermined, they are obtained based on the node coordinates:

$$\begin{array}{lll} a_i = r_j z_m - r_m z_j & b_i = z_j - z_m & c_i = r_m - r_j \\ a_j = r_m z_i - r_i z_m & b_j = z_m - z_i & c_j = r_i - r_m \\ a_m = r_i z_j - r_j z_i & b_m = z_i - z_j & c_m = r_j - r_i \end{array} \tag{A2}$$

where the position coordinates of the three nodes *i,j*, and m of an element are (r_i,z_i), (r_j,z_j), (r_m,z_m) respectively. The thermal conductivity matrix, heat capacity matrix, and temperature load vector of a thermal element are expressed as:

$$[KT]^E = \begin{bmatrix} \phi'\left(b_j^2 + c_j^2\right) & \phi'\left(b_i b_j + c_i c_j\right) & \phi'\left(b_i b_m + c_i c_m\right) \\ \phi'\left(b_i b_j + c_i c_j\right) & \phi'\left(b_j^2 + c_j^2\right) & \phi'\left(b_j b_m + c_j c_m\right) \\ \phi'\left(b_i b_m + c_i c_m\right) & \phi'\left(b_j b_m + c_j c_m\right) & \phi'\left(b_m^2 + c_m^2\right) \end{bmatrix} \tag{A3}$$

$$[NT]^E = \begin{bmatrix} \dfrac{\Delta}{30}\rho c_p(3r_i + r_j + r_m) & \dfrac{\Delta}{60}\rho c_p(2r_i + 2r_j + r_m) & \dfrac{\Delta}{60}\rho c_p(2r_i + r_j + 2r_m) \\ \dfrac{\Delta}{60}\rho c_p(2r_i + 2r_j + r_m) & \dfrac{\Delta}{30}\rho c_p(r_i + 3r_j + r_m) & \dfrac{\Delta}{60}\rho c_p(r_i + 2r_\gamma + 2r_m) \\ \dfrac{\Delta}{60}\rho c_p(2r_i + r_j + 2r_m) & \dfrac{\Delta}{60}\rho c_p(r_i + 2r_\gamma + 2r_m) & \dfrac{\Delta}{30}\rho c_p(r_i + r_j + 3r_m) \end{bmatrix} \tag{A4}$$

$$\{PT\}^E = \left[\dfrac{\Delta}{12}q_v(2r_i + r_j + r_m) \quad \dfrac{\Delta}{12}q_v(r_i + 2r_j + r_m) \quad \dfrac{\Delta}{12}q_v(r_i + r_j + 2r_m)\right]^T \tag{A5}$$

where the coefficient ϕ' is expressed as $\phi' = k(r_i + r_j + r_m)/(12\Delta)$.

Data availability

Data will be made available on request.

References

[1] C. Salpingidou, Z. Vlahostergios, D. Misirlis, S. Donnerhack, M. Flouros, A. Goulas, K. Yakinthos, Thermodynamic analysis of recuperative gas turbines and aero engines, Appl. Therm. Eng. 124 (2017) 250–260.
[2] D. Mohaddes, C.T. Chang, M. Ihme, Thermodynamic cycle analysis of superadiabatic matrix-stabilized combustion for gas turbine engines, Energy 207 (2020) 118171.
[3] T. Wang, Y. Xuan, X. Han, Investigation on hybrid thermal features of aero- engines from combustor to turbine, Int. J. Heat. Mass Transf. 200 (2023) 123559.
[4] W. Sun, T. Li, D. Yang, Q. Sun, J. Huo, Dynamic investigation of aeroengine high pressure rotor system considering assembly characteristics of bolted joints, Eng. Fail. Anal. 112 (2020) 104510.
[5] J. Hong, Z. Yang, Y. Wang, R. Cheng, Y. Ma, Combination resonances of rotor systems with asymmetric residual preloads in bolted joints, Mech. Syst. Signal. Process. 183 (2023) 109626.
[6] G. Li, S. Ding, M. Bao, H. Sun, Effect of actively managed thermal-loading in optimal design of an aeroengine turbine disk, Int. Commun. Heat Mass Transf. 81 (2017) 257–268.
[7] S. Ding, Z. Wang, G. Li, Optimal design process for aeroengine turbine disks based on energy management, J. Thermophys. Heat. Trans. 29 (4) (2015) 684–694.
[8] Y.Z. Zhao, Y.J. Chiu, C.H. Yang, G.F. Yu, Research on heat-elastic coupled vibration in a rotating rigid disk rotor system, J. Mech. Sci. Technol. 36 (4) (2022) 1667–1678.
[9] Z. Zou, L. Xuan, Y. Chen, F. Shao, Effects of flow structure on heat transfer of squealer tip in a turbine rotor blade, Int. Commun. Heat Mass Transf. 114 (2020) 104588.
[10] X. Qian, P. Yan, X. Wang, W. Han, Numerical analysis of conjugated heat transfer and thermal stress distributions in a high-temperature Ni-based superalloy turbine rotor blade, Energies. (Basel) 15 (14) (2022) 4972.
[11] J.J. Hu, B.T. An, Film-cooling effectiveness of combined hole slot geometries on a turbine rotor blade surface, Appl. Therm. Eng. 243 (2024) 122563.

[12] J.M. Owen, R.H. Roger, Flow and Heat Transfer in Rotating Disc Systems, Research Studies Press, New York, 1995.
[13] A. Lin, G. Liu, R. Chang, Y. Chen, Q. Feng, Comprehensive evaluations of heat transfer performance with conjugate heat dissipation effect in high-speed rotating free-disk system of aero-engines, Fundam. Res. 4 (3) (2022) 611–623.
[14] M. Ghasemian, M. Princevac, Y.W. Kim, H.D. Hamm, Numerical modeling of hot gas ingestion into the rotor-stator disk cavities of a subscale 1.5-stage axial gas turbine, Int. J. Heat. Mass Transf. 130 (2019) 1016–1031.
[15] J.M. Owen, C.A. Long, Review of buoyancy-induced flow in rotating cavities, J. Turbomach. 137 (11) (2015) 111001.
[16] A. Lin, G. Liu, X. Yu, R. Chang, Q. Feng, Comprehensive investigations on fluid flow and heat transfer characteristics of a high-speed rotating turbine disk cavity system of aero-engine, Int. Commun. Heat Mass Transf. 136 (2022) 106170.
[17] G.L. Liao, L.J. Liu, F. Zhang, J.Q. E, J.W. Chen, A comparison of numerical investigations on the flow and heat transfer characteristics in the rotor-stator cavity, Appl. Therm. Eng. 162 (2019) 114231.
[18] V. Mudavath, V. Arumuru, Impingement heat transfer characteristics of nozzles with inclined exits, Exp. Heat Transf. 37 (6) (2023) 541–556.
[19] A. Ma, Q. Wu, T. Zhou, R. Hu, Effect of inlet flow ratio on heat transfer characteristics of a novel twin-web turbine disk with receiving holes, Case Stud. Therm. Eng. 34 (2022) 101990.
[20] X. Yang, Z. Ren, X. Li, J. Ren, P.M. Ligrani, Flow and heat transfer characteristics in a pre-swirl rotor-stator cavity, Int. J. Therm. Sci. 172 (2022) 107271.
[21] A. Ma, F. Liu, T. Zhou, R. Hu, Numerical investigation on heat transfer characteristics of twin-web turbine disk-cavity system, Appl. Therm. Eng. 184 (2021) 116268.
[22] X. Luo, L. Wang, X. Zhao, G. Xu, H. Wu, Experimental investigation of heat transfer in a rotor–stator cavity with cooling air inlet at low radius, Int. J. Heat. Mass Transf. 76 (2014) 65–80.
[23] S. Choi, P. Choi, H.S. Sohn, D.H. Rhee, H.H. Cho, Local heat and mass transfer in a rotor-stator system with hub inflow: thermal boundary layer and superposition effect, Int. Commun. Heat Mass Transf. 144 (2023) 106799.
[24] B. Hu, X.S. Li, Y.X. Fu, F. Zhang, C.W. Gu, X.D. Ren, C. Wang, Experimental investigation on the flow and flow-rotor heat transfer in a rotor-stator spinning disk reactor, Appl. Therm. Eng. 162 (2019) 114316.
[25] A. Lin, J. Ma, G. Fan, Z. Lei, H. Fawzy, G. Liu, Aerothermal performances of a rotating turbine disk cavity with non-uniform wall temperature profiles in an aero-engine, Therm. Sci. Eng. Prog. 38 (2023) 101582.
[26] R. Chang, Y. Zhao, M. Guo, A. Lin, Y. Wang, G. Liu, Dimensionless analysis of flow and heat transfer characteristics in a high-speed rotor–stator disk cavity based on similarity criteria, Appl. Therm. Eng. 238 (2024) 122148.
[27] G. Creci, M.T. De Mendoça, J.C. Menezes, J.R. Barbosa, Heat transfer analysis in a single spool gas turbine by using calculated-estimated coefficients with the finite element method, Appl. Sci. 10 (23) (2020) 8328.
[28] A. Rajeev, V. Puneeth, S. Manjunatha, O.D. Makinde, Magnetohydrodynamic flow of two immiscible hybrid nanofluids between two rotating disks, Numer. Heat Transf. Part A Appl. (2024) 1–19, 0 (0).
[29] Z. Li, Y.G. Li, S. Sampath, Aeroengine transient performance simulation integrated with generic heat soakage and tip clearance model, Aeronaut. J. 126 (2022) 1–23.
[30] Y.Z. Zhao, J. Zhou, M.J. Guo, Y.P. Xu, Equivalent thin-layer temperature field model (ETTM) for bolted rotors to describe interface temperature jump, Int. J. Heat. Mass Transf. 222 (2024) 0017–9310.
[31] F.F. Wang, X.T. Zhao, J.H. Liu, Q.X. Ma, J. Sun, S.X. Xu, Z.Q. Han, Study on the relationship between interfacial heat transfer coefficient and interface pressure in squeeze casting by using microscopic contact model, Int. J. Therm. Sci. 152 (2020) 106300.
[32] F.F. Wang, X.Y. Wang, Z.Q. Han, On the interfacial heat transfer and pressure transmission in squeeze casting: a case study of the sensitivity to materials, Int. J. Heat. Mass Transf. 133 (2019) 52–61.
[33] F.F. Wang, Q.X. Ma, W. Meng, Z.Q. Han, Experimental study on the heat transfer behavior and contact pressure at the casting-mold interface in squeeze casting of aluminum alloy, Int. J. Heat. Mass Transf. 112 (2017) 1032–1043.
[34] L. Qiu, X. Zhang, Z. Guo, Q. Li, Interfacial heat transport in nano-carbon assemblies, Carbon. N. Y. 178 (2021) 391–412.
[35] X. Yu, Y. Sun, S. Wu, Two-dimensional contact of asperities to multi-stage contact between curved fractal surfaces based on attitude angle, Tribol. Int. 189 (2023) 108989.
[36] Y.M. Yang, T. Nikolaidis, S. Jafari, P. Pilidis, Gas turbine engine transient performance and heat transfer effect modelling: a comprehensive review, research challenges, and exploring the future, Appl. Therm. Eng. 236 (2024) 121523.